Post-Perovskite Phase Transition in the Pyrolitic Lowermost Mantle: Implications for Ubiquitous Occurrence of Post-Perovskite Above CMB

Yasuhiro Kuwayama[1], Kei Hirose[1,2], Laura Cobden[3], Mayu Kusakabe[1], Shigehiko Tateno[2], and Yasuo Ohishi[4]

[1]Department of Earth and Planetary Science, The University of Tokyo, Tokyo, Japan
[2]Earth-Life Science Institute, Tokyo Institute of Technology, Tokyo, Japan
[3]Department of Earth Sciences, Utrecht University, Utrecht, The Netherlands
[4]Japan Synchrotron Radiation Research Institute, SPring-8, Hyogo, Japan

Key Points:

- We conducted synchrotron XRD measurements of a pyrolitic mantle material up to 4480 K at 122–166 GPa in a laser-heated diamond-anvil cell.
- Phase transition between bridgmanite and post-perovskite occurs in pyrolite within the lowermost mantle pressure range even at >4000 K.
- Ubiquitous occurrence of post-perovskite above the CMB is consistent with recent high-quality seismological observations of D" reflections.

Abstract We conducted X-ray diffraction (XRD) measurements of a pyrolitic mantle material up to 4480 K at 122–166 GPa in a laser-heated diamond-anvil cell (DAC). Results demonstrate that the phase transition between bridgmanite and post-perovskite occurs in pyrolite within the lowermost mantle pressure range even at >4000 K. It suggests the ubiquitous occurrence of post-perovskite above the core-mantle boundary (CMB), which may be consistent with recent high-quality seismology data that non-observations of D" reflections are exceptions. Combining with earlier experiments performed at and below the normal lower-mantle geotherm, our data show that the bridgmanite + post-perovskite two-phase region is ~5 GPa thick and the Clapeyron slope of the boundary is $+7^{+2}_{-3}$ MPa/K in agreement with previous theoretical calculations. The global presence of rheologically weak post-perovskite at the bottom of the mantle has profound implications in seismology, geodynamics, and heat transfer from the core.

Plain Language Summary (Al, Fe)-bearing $MgSiO_3$ bridgmanite is a predominant mineral in the lower mantle. While bridgmanite with $MgSiO_3$ end-member composition is known to undergo a phase transition to post-perovskite at lowermost mantle pressures,

the pressures and thickness of the phase boundary in a typical mantle material (pyrolite) have been controversial. The present synchrotron XRD measurements of pyrolite performed up to 4480 K around the CMB pressure show that the bridgmanite/post-perovskite phase transition takes place within the lowermost mantle pressure range even under high temperatures of the CMB region. The bridgmanite + post-perovskite two-phase region is found to be about 90 km thick. These results suggest the global presence of post-perovskite above the CMB, which is consistent with recent seismological observations of D" reflectors not only in the circum-Pacific high velocity regions but also in many areas away from subduction zones. Post-perovskite is rheologically weak, and its ubiquitous occurrence in the lowermost mantle has important seismological and geodynamical implications. The high positive pressure/temperature slope ($+7^{+2}_{-3}$ MPa/K) of the boundary suggests that a phase transition to bridgmanite assists upwelling of plumes from hot regions above the CMB.

1. Introduction

Both experiments and theory have shown that a phase transition between bridgmanite (perovskite-type structure) and post-perovskite occurs in $MgSiO_3$ end-member under the lowermost mantle conditions (~120 GPa and ~2400 K), where the D" seismic velocity discontinuity is observed (Murakami et al., 2004; Oganov & Ono, 2004; Tateno et al., 2009). The Clapeyron slope of the phase boundary in $MgSiO_3$ was determined to be +8–13 MPa/K, several times larger in magnitude than those of major upper mantle phase transitions. The pressures and sharpness of the post-perovskite phase transition have been examined also in a pyrolitic mantle material. In a natural mantle, Al and Fe impurities (e.g., Tateno et al., 2005; Mao et al., 2005; Hirose et al., 2008; Catalli et al., 2009) and the coexistence with ferropericlase (Sinmyo et al., 2011) affect the transition pressure and broaden a pressure interval of transition (see a review by Hirose et al., 2015). It has been repeatedly reported the post-perovskite phase transition occurs in a pyrolitic lowermost mantle around 120 GPa, comparable to the case in pure $MgSiO_3$, along the normal lower-mantle geotherm with a ~5 GPa pressure interval (Murakami et al., 2005; Ono & Oganov, 2005; Ohta et al., 2008). On the other hand, the similar XRD study by Grocholski et al. (2012) found higher transition pressure that is beyond the pressure range of the Earth's mantle and much broader pressure interval (140–168 GPa at 2500 K).

In these previous experimental studies on pyrolite, however, the stabilities of bridgmanite and post-perovskite have been explored only up to 2700 K under the lowermost mantle conditions. There are more observations of the D" seismic discontinuity in seismically

fast regions associated with paleo-subduction than in slow regions—although this may be influenced by favorable earthquake source and receiver combinations—and in some locations the D" discontinuity is not observed at all (see reviews by Wysession et al., 1998, Cobden et al., 2015, and Jackson & Thomas, 2021). The high Clapeyron slope of the bridgmanite to post-perovskite phase transition might suggest that bridgmanite is stable (post-perovskite is absent) to the CMB in relatively hot areas. Even in cold regions, "paired" discontinuities (positive S-wave velocity jump at the D" discontinuity and negative one at a deeper level near the CMB) might indicate the presence of bridgmanite above the CMB, instead of post-perovskite, as a consequence of back transformation from post-perovskite to bridgmanite at high temperatures in a thermal boundary layer (a double-crossing scenario) (Thomas et al., 2004; Hernlund et al., 2005). It is of great importance to verify these scenarios by phase equilibria experiments on multi-phase assemblages that are representative of average mantle material under high temperatures of the CMB region. In addition, the Clapeyron slope of the bridgmanite/post-perovskite boundary was determined to be +5 to +13 MPa/K in $MgSiO_3$ end-member by theories (Tsuchiya et al., 2004; Oganov & Ono, 2004) and experiments (Ono & Oganov, 2005; Hirose et al., 2006; Tateno et al., 2009). It is several times larger in magnitude than those of major upper mantle phase transitions, suggesting that the post-perovskite transition has important dynamical consequences (Nakagawa & Tackley, 2004; Tackley et al., 2007). The high positive Clapeyron slope was reported also for pyrolite, but it was constrained by experiments performed in narrow temperature ranges less than ~1000 K (Ono & Oganov, 2005; Ohta et al., 2008; Grocholski et al., 2012).

Here we performed synchrotron XRD measurements of a pyrolitic mantle material to investigate the post-perovskite phase transition at high temperatures (3570 K and higher) including those above its solidus temperature. The results show that bridgmanite/post-perovskite phase transition occurs within the lowermost pressure range even at >4000 K. Combining with the earlier experimental results by Ohta et al. (2008), the post-perovskite-in and bridgmanite-out curves are constrained by data obtained in a wide temperature range from 1780 to 4480 K, and the Clapeyron slope is found to be $+7^{+2}_{-3}$ MPa/K when the gold pressure scale proposed by Fei et al. (2007) is applied. These results suggest that post-perovskite is present globally above the CMB, which may be consistent with recent high-quality seismological data that non-observations of D" reflection are exceptional (Jackson & Thomas, 2021).

2. Experimental Methods

High-pressure and -temperature (*P-T*) experiments were performed with *in-situ* XRD measurements in a laser-heated DAC. We employed a symmetric-type DAC with beveled 90-μm culet diamond anvils. A starting material was the same as that used in Ohta et al. (2008); it was prepared from gel with the chemical composition of a natural peridotite KLB-1, similar to pyrolite (Takahashi, 1986). The sample was mixed with fine gold powder and loaded into a hole at the center of a pre-indented rhenium gasket. Argon was cryogenically loaded and used as a thermal insulator.

After compression, heating was performed from both sides of the sample using a couple of 100 W single-mode Yb fiber lasers (SPI Lasers Co. Ltd.) with beam shaping optics that converts a beam with a Gaussian intensity distribution to one with a flat-top distribution. The laser spot size was approximately 30 μm across. Heating duration was 3 sec. One-dimensional radial temperature profile across a hot spot was obtained by a spectro-radiometric method (e.g., Tateno et al., 2018a) (Figure 1). In runs #1–3 in which the sample was partially molten, temperature shown in Table 1 corresponds to that at the boundary between a melt pool and a solid layer, which was determined by a combination of the temperature profile and a melting texture found in a cross section of a recovered sample (e.g., Hasegawa et al., 2021). For subsolidus experiments (runs #4 and #5), sample temperatures are the average in a 6 μm region at the hot spot, from which XRD data were collected. The overall temperature uncertainty may be ±5% according to Mori et al. (2017). The sample was heated only once in each run. Pressure at high temperature was determined based on the unit-cell volume of gold (Fei et al., 2007). Those in the earlier experiments performed by Ohta et al. (2008) were based on the equation of state (EoS) of gold proposed by Hirose et al. (2008), which is not applicable at high temperatures like ~4000 K. Therefore, we recalculated the pressures in Ohta et al. (2008) using the Mie-Grüneisen-Debye EoS of gold proposed by Fei et al. (2007), in order to compare their results with those obtained in this study (Table 1).

Angle-dispersive XRD patterns were collected *in-situ* at high *P-T* at the beamline BL10XU, SPring-8 synchrotron radiation facility (Hirao et al., 2020) (Figure 2). A monochromatic incident X-ray beam was focused by stacked compound refractive lenses and collimated to approximately 6 μm area (full width at half maximum) on a sample. The wavelength was 0.4133 to 0.4158 Å (~30 keV). XRD data were obtained continuously during heating on a digital flat panel X-ray detector (Perkin Elmer) with exposure time of 1 sec. To obtain conventional 1D diffraction patterns, 2D XRD images were integrated as a function of 2θ angle (Seto et al., 2010).

After high *P*-*T* experiments, samples in runs #1–3 were recovered from a DAC, and their cross sections across the center of a laser-heated spot were prepared parallel to the compression axis by using a focused Ga ion beam (FIB) (FEI, Versa3D DualBeam). X-ray elemental maps were obtained with an energy-dispersive X-ray spectrometry (EDS) attached with a field-emission-type scanning electron microscope (FE-SEM) in the dual beam FIB system (Figure 1).

3. Results

We have conducted five separate high *P*-*T* experiments on a pyrolitic mantle material up to 156 GPa and 3570 K (Table 1). In order to avoid kinetic hindering of phase transformation especially in such a multi-component system, heating was made on an amorphous starting material at a single *P*-*T* condition in each run. In run #1, the sample was compressed and then heated to 3910 K at 122 GPa, higher than the solidus temperature of pyrolite (Nomura et al., 2014; Kim et al., 2020) (Figure 3a). The XRD spectrum collected *in-situ* during heating shows that bridgmanite and minor post-perovskite, in addition to ferropericlase and $CaSiO_3$ perovskite, grew from the amorphous sample (Figure 2a). Microprobe analyses of the cross section of this sample recovered from high pressure demonstrate that there is a round pocket of quenched melt at the center, being enriched in Fe and Ca and depleted in Si (Figure 1). This melt pocket is surrounded by a Si-rich and (Fe, Ca)-poor layer, which should represent bridgmanite (± post-perovskite) observed in the high *P*-*T* XRD pattern. It indicates that bridgmanite is the liquidus phase, consistent with the earlier melting experiments on pyrolite performed by Tateno et al. (2014).

Similar experiments were made in runs #2 and #3 at conditions slightly higher in both *P* and *T* (Figure 3a). Diffuse scattering signals from melt are recognized in their *in-situ* XRD patterns (Fiquet et al., 2010), in particular for run #2 (Figure 2b). The XRD data indicate that melt coexisted with bridgmanite and minor ferropericlase (post-perovskite is absent) in run #2 at 128 GPa and 4480 K. In contrast, the high *P*-*T* XRD pattern is dominated by post-perovskite in run #3 performed at 130 GPa and 4300 K (Figure 2c). In addition, runs #4 and #5 were conducted at 156–166 GPa and 3570–3860 K under subsolidus conditions (Figure 3a), which is supported by observations that the number of peaks and their relative intensities in XRD patterns did not change upon quenching temperature.

These results of runs #1–3 tightly constrain the post-perovskite-in and bridgmanite-out conditions around 4000 K (Figure 3a). While partial melts coexisted with both

bridgmanite and post-perovskite in runs #1 and 3, either one of them was dominant in these experiments (Figures 2a and 2c), indicating that their *P*-*T* conditions should be close to the post-perovskite-in and bridgmanite-out curves, respectively. The width of the post-perovskite phase transition should thus be about 5 GPa, corresponding to a lowermost mantle depth range of 90 km, similar to that observed by Ohta et al. (2008) at lower temperatures below 2550 K. When combined with Ohta et al. (2008)'s data (Table 1), our results obtained in a wide temperature range from 1780 to 4480 K at 108–130 GPa show the Clapeyron slope of these post-perovskite-in and bridgmanite-out curves to be $+7^{+2}_{-3}$ MPa/K, although the slope should change at the solidus curve (Figure 3a).

4. Discussion

4.1. Post-Perovskite Phase Transition in Pyrolitic Lowermost Mantle

Both the pressure (~120 GPa at 2400 K) and Clapeyron slope of the post-perovskite phase transition boundary we obtained for pyrolite are in agreement with those for $MgSiO_3$ end-member reported by earlier *ab initio* calculations (Tsuchiya et al., 2004; Oganov & Ono, 2004). While the experiments on pyrolite carried out by Grocholski et al. (2012) found the phase transition at 140–168 GPa and 2500 K, earlier XRD measurements including those by another group have repeatedly demonstrated that it takes place around 120 GPa (Murakami et al., 2005; Ono & Oganov, 2005; Ohta et al., 2008) along the normal lower-mantle geotherm (Brown & Shankland, 1981). Such a large discrepancy is not reconciled with the difference in pressure scale employed to determine experimental pressures in these studies, although pressure estimates can change as much as 15 GPa in the relevant pressure range, depending on choices of an internal pressure standard and its equation of state (see a review by Hirose et al., 2015) (Figure 3b). The difference in a pressure medium is also unlikely to be an important source of the discrepancy; noble gas (argon or neon) pressure medium was used in Ono & Oganov (2005) and this study as well as in Grocholski et al. (2012).

The Clapeyron slope of $+7^{+2}_{-3}$ MPa/K depends on the choice of the Au pressure scale. When different EoSs of gold (Jamieson et al., 1982; Anderson et al., 1989; Shim et al., 2002; Tsuchiya, 2003) other than the Fei et al. (2007)'s EoS are employed, the slope becomes smaller ranging from +3 to +7 MPa/K (Figure 3b). The pressures of the transition also becomes lower. The slope of $+7^{+2}_{-3}$ MPa/K found in pyrolite is markedly smaller than +13±1 MPa/K in $MgSiO_3$ (Tateno et al., 2009), which could be because of the effects of Al and Fe impurities included in natural samples.

The present experiments and the earlier ones by Ohta et al. (2008) demonstrate that bridgmanite and post-perovskite coexist in a pyrolitic mantle material in a ~5 GPa pressure interval at ~4000 K and ~2000–2500 K, respectively (Figure 3a). The thickness of the bridgmanite + post-perovskite two-phase region has been reported to be wider, more than 20 GPa in (Al, Fe)-bearing $MgSiO_3$ (Catalli et al., 2009; Andrault et al., 2010). Nevertheless, bridgmanite/post-perovskite coexists with (Mg,Fe)O ferropericlase in pyrolite, and the partitioning of FeO with ferropericlase results in lower FeO concentration in post-perovskite than in bridgmanite. It leads to a much narrower bridgmanite + post-perovskite two-phase region in pyrolite than that in the (Al, Fe)-bearing $MgSiO_3$ system (Sinmyo et al., 2011) as observed in this study as well as in Ohta et al. (2008).

4.2. Ubiquitous Occurrence of Post-Perovskite above CMB

These results show that post-perovskite transforms into bridgmanite above 4800 K at the CMB (Figure 3). It is much higher than the present-day CMB temperature, while its estimates range from 3600 to 4300 K (e.g., Lay et al., 2008; Nomura et al., 2014; Kim et al., 2020). If the deep lower mantle is dominated by a pyrolitic material, it suggests that 1) the bridgmanite/post-perovskite phase transition takes place globally in the lowermost mantle although the transition is not sharp, and 2) post-perovskite is present ubiquitously above the CMB. This conclusion does not depend on the choice of the EoS of gold to determine experimental pressures (Figure 3b). If the lower mantle is not pyrolitic but more enriched in silica and therefore poor in (Mg,Fe)O ferropericlase (Murakami et al., 2012; Mashino et al., 2020), the *P*-*T* location of the post-perovskite-in curve does not change as long as the chemical composition of bridgmanite is similar (Figure 3a), while the bridgmanite + post-perovskite two-phase coexisting region should be wider (Sinmyo et al., 2011).

The ~5 GPa pressure width of the bridgmanite + post-perovskite coexistence corresponds to ~90 km depth interval in the lowermost mantle. The sharpness of the D" seismic discontinuity should be less than this (Weber et al., 1996) and potentially as narrow as 8–30 km (i.e. <2 GPa) (Lay & Young, 1989; Lay, 2008; Wysession et al., 1998), suggesting that the bridgmanite/post-perovskite transition boundary in pyrolite may not be observed as a seismic velocity discontinuity as argued by Lay (2008).

The D" discontinuity is found mainly in high-velocity regions underneath the circum-Pacific (Wysession et al., 1998; Cobden et al., 2015; Jackson & Thomas, 2021), and this

has been attributed to the enrichment in subducted depleted mantle materials (harzburgitic rocks), in which the bridgmanite to post-perovskite phase transition occurs in a narrow pressure range because they are poor in Al and Fe impurities (Grocholski et al., 2012). D" seismic reflections could also be produced in these regions by scattering off chemical heterogeneities (e.g., Cobden & Thomas, 2013). On the other hand, there are observations of the D" discontinuity beneath the central Pacific as well (Lay et al., 2006; Cobden & Thomas, 2013; Jackson & Thomas, 2021). Post-perovskite should be predominant above the CMB including such areas away from the circum-Pacific high-velocity regions. Our results do not preclude the bridgmanite/post-perovskite transition in pyrolite from generating D" reflections; stress-induced re-equilibration within the two-phase region can produce high amplitude seismic reflections, even when the transition region is thick (Langrand et al., 2019). Additionally, development of the lattice-preferred orientation of post-perovskite may generate sharp reflectors within a broad two-phase region (Ammann et al., 2010; Pisconti et al., 2019).

Indeed, the ubiquitous occurrence of post-perovskite above the CMB has been supported by statistical analyses of seismic observations (Cobden et al., 2012, 2015) and by comparisons between seismic tomography and geodynamic models (Koelemeijer et al., 2018). Mineral physics models with post-perovskite are compatible with both global and local seismic data of S- and P-wave velocity perturbations in the lowermost mantle rather than post-perovskite-free models. Recent high-quality seismological data indicate that non-observations of a discontinuity in the lowermost mantle are not common but exceptional (Jackson & Thomas, 2021).

The ubiquitous presence of post-perovskite above the CMB has profound geodynamical consequences. Because of its proximity to the CMB, the global occurrence of the bridgmanite/post-perovskite phase transition with high positive Clapeyron slope ($+7^{+2}_{-3}$ MPa/K) destabilizes the thermal boundary layer developed at the bottom of the mantle and enhances plume upwelling (Nakagawa & Tackley, 2004; Li et al., 2014; Hirose et al., 2015). Theoretical calculations and experiments demonstrated that post-perovskite is at least five times weaker than bridgmanite (Hunt et al., 2009; Ammann et al., 2010). The low-viscosity D" layer allows cold slab materials to spread extensively above the CMB, leading to an increase in heat transfer from the core (Buffett, 2007; Cizkova et al., 2010). It also enhances the segregation of MORB crust materials from the rest of the subducted slab, contributing to the formation of dense piles above the CMB (Nakagawa & Tackley, 2011).

Ultralow-velocity zones are observed locally above the CMB, likely representing partially molten materials with relatively low melting temperatures such as FeO-rich ones (Boukaré et al., 2015; Helffrich et al., 2020). On the other hand, when the CMB temperature was higher in the past (Labrosse, 2015), the lowermost mantle could have been globally molten. The present experiments demonstrate that post-perovskite is the liquidus phase (the first phase to appear upon crystallization) in a pyrolitic lowermost mantle (Tateno et al., 2014) (Figure 3). The behaviors of trace elements during partial melting involving post-perovskite may be different from that with bridgmanite at shallower depths; water and Na_2O have been shown to be partitioned more into Al-bearing post-perovskite than into bridgmanite (Townsend et al., 2016; Hirose et al., 2005; Tateno et al., 2018b). Partitioning of trace elements between melt and post-perovskite is yet to be explored.

5. Conclusions

We have examined the phase transition between bridgmanite and post-perovskite in a pyrolitic mantle material at high temperatures (3570–4480 K) around the CMB pressure. Results demonstrate that the bridgmanite/post-perovskite phase transition occurs in pyrolite within the lowermost mantle pressure range even at >4000 K. They also indicate the two-phase coexisting region of ~5 GPa and the Clapeyron slope of $+7^{+2}_{-3}$ MPa/K, when combined with earlier experimental results obtained at lower temperatures (Ohta et al., 2008).

The global presence of post-perovskite above the CMB is consistent with recent high-quality seismological observations of the D" seismic reflections; they are found not only in the circum-Pacific high-velocity regions but also in many places away from such (presumably) cold areas (Jackson & Thomas, 2021). The 5 GPa two-phase coexisting interval may be too thick for the bridgmanite/post-perovskite phase transition in pyrolite to be the cause of seismic reflections. Alternatively the seismic discontinuity observed underneath subduction zones could be attributed to the post-perovskite phase transition in depleted peridotite materials that should be abundant in such areas (Grocholski et al., 2012) or caused by scattering off chemical heterogeneities that derive from subductions of former oceanic plates (Cobden & Thomas, 2013). The D" reflections observed in areas distant from subduction zones can be formed by other mechanisms such as deformation of weak post-perovskite within a two-phase region (Ammann et al., 2010; Pisconti et al., 2019). Indeed, the ubiquitous occurrence of post-perovskite above the CMB is supported by a statistical interpretation of seismic observations (Cobden et al., 2012, 2015) and by

comparisons of seismic tomographies between observed and synthesized from geodynamic simulations (Koelemeijer et al., 2018). The global presence of rheologically weak post-perovskite at the bottom of the mantle has profound implications for the dynamics and thermal histories of both the mantle and the core.

Data Availability Statement

Datasets for this research are found in Table 1 available online (from https://zenodo.org/record/5513281).

Acknowledgments

K. Yonemitsu is acknowledged for her help in FIB/SEM/EDS analyses. XRD measurements were carried out at BL10XU, SPring-8 (proposals no. 2019B0072 and 2020A0072). This work was supported by the JSPS grants 16H06285 and 21H04968 to K.H.

References

Ammann, M. W., Brodholt, J. P., Wookey, J., & Dobson, D. P. (2010). First-principles constraints on diffusion in lower-mantle minerals and a weak D" layer. *Nature*, *465*, 462–465. http://dx.doi.org/10.1038/nature09052

Anderson, O. L., Isaak, D. G., & Yamamoto, S. (1989). Anharmonicity and the equation of state for gold. *Journal of Applied Physics*, *65*, 1534–1543. https://doi.org/10.1063/1.342969

Andrault, D., Muñoz, M., Bolfan-Casanova, N., Guignot, N., Perrillat, J.-P., Aquilanti, G., & Pascarelli, S. (2010). Experimental evidence for perovskite and post-perovskite coexistence throughout the whole D" region. *Earth and Planetary Science Letters*, *293*, 90–96. https://doi.org/10.1016/j.epsl.2010.02.026

Boukaré, C.-E., Ricard, Y., & Fiquet, G. (2015). Thermodynamics of the MgO-FeO-SiO_2 system up to 140 GPa: application to the crystallization of Earth's magma ocean. *Journal of Geophysical Research: Solid Earth*, *120*, 6085–6101. https://doi.org/10.1002/ 2015JB011929

Brown, M. J., & Shankland, T. J. (1981). Thermodynamic parameters in the Earth as determined from seismic profiles. *Geophysical Journal Royal Astronomical Society*, *66*, 579–596.

Buffett, B. A. (2007). A bound on heat flow below a double crossing of the perovskite-postperovskite phase transition. *Geophysical Research Letters*, *34*, L17302. doi:10.1029/2007GL030930

Catalli K., Shim S. H., & Prakapenka, V. (2009). Thickness and Clapeyron slope of the post-perovskite boundary. *Nature*, *462*, 782–785. https://doi.org/10.1038/nature08598

Cizkova, H., Cadek, O., Matyska, C., &, Yuen, D. A. (2010). Implications of post-perovskite transport properties for core–mantle dynamics. *Physics of Earth and Planetary Interiors*, *180*, 235–243. https://doi.org/10.1016/j.pepi.2009.08.008

Cobden, L., & Thomas, C. (2013). The origin of D" reflections: a systematic study of seismic array data sets. *Geophysical Journal International, 194,* 1091–1118. https://doi.org/10.1093/gji/ggt152

Cobden, L., Mosca, I., Trampert, J., & Ritsema, J. (2012). On the likelihood of post-perovskite near the core-mantle boundary: a statistical interpretation of seismic observations. *Physics of the Earth and Planetary Interiors, 210–211,* 21–35. http://dx.doi.org/10.1016/j.pepi.2012.08.007

Cobden, L., Thomas, C., & Trampert, J. (2015). Seismic detection of post-perovskite inside the Earth. In A. Khan, F. Deschamps (Eds.), *The Earth's Heterogeneous Mantle* (pp. 391–440). Switzerland: Springer Geophysics. DOI: 10.1007/978-3-319-15627-9_13

Fei, Y., Ricolleau, A., Frank, M., Mibe, K., Shen, G., & Prakapenka, V. (2007) . Toward an internally consistent pressure scale. *Proceedings of the National Academy of Sciences of the United States of America*, *104*, 9182–9186. https://doi.org/10.1073/pnas.0609013104

Fiquet, G., Auzende, A. L., Siebert, J., Corgne, A., Bureau, H., Ozawa, H., & Garbarino, G. (2010). Melting of peridotite to 140 Gigapascals. *Science*, *329*, 1516–1518. DOI: 10.1126/science.1192448

Grocholski, B., Catalli, K., Shim, S-H., & Prakapenka, V. (2012). Mineralogical effects on the detectability of the postperovskite boundary. *Proceedings of the National Academy of Sciences of the United States of America*, *109*, 2275–2279. https://doi.org/10.1073/pnas.1109204109

Hasegawa, M., Hirose, K., Oka, K., & Ohishi, Y. (2021). Liquidus phase relations and solid-liquid partitioning in the Fe-Si-C system under core pressures. *Geophysical Research Letters*, *48*, e2021GL092681. https://doi.org/10.1029/2021GL092681

366 Helffrich, G., Hirose, K., & Nomura, R. (2020). Thermodynamical modeling of liquid
367 Fe-Si-Mg-O: molten magnesium silicate release from the core. *Geophysical Research*
368 *Letters*, *47*, e2020GL089218. https://doi.org/10.1029/2020GL089218
369 Hernlund, J. W., Thomas, C., & Tackley, P. J. (2005). A doubling of the postperovskite
370 phase boundary and structure of the Earth's lower mantle. *Nature*, *434*, 882–886.
371 https://doi.org/10.1038/nature03472
372 Hirao, N., Kawaguchi, S., Hirose, K., Shimizu, K., Ohtani, E., & Ohishi, Y. (2020). New
373 developments in high-pressure X-ray diffraction beamline for diamond anvil cell at
374 SPring-8. *Matter and Radiation at Extremes*, *5*, 018403.
375 https://doi.org/10.1063/1.5126038
376 Hirose, K., Takafuji, N., Sata, N., & Ohishi, Y. (2005). Phase transition and density of
377 subducted MORB crust in the lower mantle. *Earth and Planetary Science Letters*, *237*,
378 239–251. http://dx.doi.org/10.1016/j.epsl.2005.06.035
379 Hirose, K., Sinmyo, R., Sata, N., & Ohishi, Y. (2006). Determination of post-perovskite
380 phase transition boundary in $MgSiO_3$ using Au and MgO internal pressure standards.
381 *Geophysical Research Letters*, *33*, L01310.
382 http://dx.doi.org/ 10.1029/2005GL024468
383 Hirose, K., Takafuji, N., Fujino, K., Shieh, S. R., & Duffy, T. S., (2008). Iron partitioning
384 between perovskite and post-perovskite: A transmission electron microscope study.
385 *American Mineralogist*, *93*, 1678–1681. http://dx.doi.org/10.2138/am.2008.3001
386 Hirose, K., Sata, N., Komabayashi, T., & Ohishi, Y. (2008). Simultaneous volume
387 measurements of Au and MgO to 140 GPa and thermal equation of state of Au based
388 on MgO pressure scale. *Physics of the Earth and Planetary Interiors*, 167, 149–154.
389 https://doi.org/10.1016/j.pepi.2008.03.002
390 Hirose, K., Wentzcovitch, R., Yuen, D., & Lay, T. (2015). Mineralogy of the deep mantle
391 – the post-perovskite phase and its geophysical significance. In G. Schubert (Ed.),
392 *Treatise on Geophysics*, 2nd edition (Vol. 2, pp. 85–115). Oxford: Elsevier.
393 https://doi.org/10.1016/B978-0-444-53802-4.00054-3
394 Hunt, S. A., Weidner, D. J., Li, L., Wang, L., Walte, N. P., Brodholt, J. P., & Dobson, D.
395 P. (2009). Weakening of calcium iridate during its transformation from perovskite to
396 post-perovskite. *Nature Geosciences, 2*, 794–797. DOI: 10.1038/NGEO663
397 Jackson, J. M., & Thomas, C. (2021). Seismic and mineral physics constraints on the D"
398 Layer. In H. Marquardt, M. Ballmer, S. Cottaar, J. Konter (Eds.), *Mantle convection*
399 *and surface expressions, Geophysical Monograph Series* (Vol. 263, pp. 193–227).
400 Washington, DC: John Wiley & Sons, Inc. DOI: 10.1002/9781119528609.ch8

401 Jamieson, J. C., Fritz, J. N., & Manghnani, M. H. (1982). Pressure measurement at high
402 temperature in x-ray diffraction studies: gold as a primary standard. In S. Akimoto,
403 M.H. Manghnani (Eds.), *High-pressure research in geophysics* (pp. 27–48). Tokyo:
404 CAPJ.
405 Kim, T., Ko, B., Greenberg, E., Prakapenka, V., Shim, S-H., & Lee, Y. (2020). Low
406 melting temperature of anhydrous mantle materials at the core-mantle boundary.
407 *Geophysical Research Letters*, *47*, e2020GL089345.
408 https://doi.org/10.1029/2020GL089345
409 Koelemeijer, P., Schuberth, B. S. A., Davies, D. R., Deuss, A., & Ritsema, J. (2018).
410 Constraints on the presence of post-perovskite in Earth's lowermost mantle from
411 tomographic-geodynamic model comparisons. *Earth and Planetary Science Letters*,
412 *494*, 226–238. https://doi.org/10.1016/j.epsl.2018.04.056
413 Labrosse, S. (2015). Thermal evolution of the core with a high thermal conductivity.
414 *Physics of the Earth and Planetary Interiors.* 247, 36–55.
415 https://doi.org/10.1016/j.pepi.2015.02.002
416 Langrand, C., Andrault, D., Durand, S., Konôpková, Z., Hilairet, N., Thomas, C., &
417 Merkel, S. (2019). Kinetics and detectability of the bridgmanite to post-perovskite
418 transformation in the Earth's D" layer. *Nature communications*, *10*, 5680.
419 https://doi.org/10.1038/s41467-019-13482-x
420 Lay, T. (2008). Sharpness of the D" discontinuity beneath the Cocos Plate: implications
421 for the perovskite to post-perovskite phase transition. *Geophysical Research Letters*,
422 *35*, L03304. http://dx.doi.org/10.1029/2007GL032465
423 Lay, T. & Young, C. J. (1989). Waveform complexity in teleseismic broadband SH
424 displacements: Slab diffractions or deep mantle reflections? *Geophysical Research*
425 *Letters*, *16*, 605–608.
426 https://deepblue.lib.umich.edu/bitstream/handle/2027.42/95458/grl4356.pdf?sequen
427 ce=1&isAllowed=y
428 Lay, T., Hernlund, J., Garnero, E. J., & Thorne, S. (2006) . A post-perovskite lens and D"
429 heat flux beneath the central Pacific. *Science*, *314*, 1272–1276.
430 DOI: 10.1126/science.1133280
431 Lay, T., Hernlund, J., & Buffett, B. A. (2008). Core–mantle boundary heat flow. *Nature*
432 *Geoscience*, *1*, 25–32. DOI:10.1038/ngeo.2007.44
433 Li, Y., Deschamps, F. & Tackley, P. J. (2014). Effects of low-viscosity post-perovskite
434 on the stability and structure of primordial reservoirs in the lower mantle. *Geophysical*
435 *Research Letters*, *41*, 7089–7097. doi: 10.1002/2014GL061362

Mao, W. L., Meng, Y., Shen, G., Prakapenka, V. B., Campbell, A. J., Heinz, et al. (2005). Iron-rich silicates in the Earth's D" layer. *Proceedings of the National Academy of Sciences of the United States of America*, *102*, 9751–9753. doi: 10.1073/pnas.0503737102

Mashino, I., Murakami, M., Miyajima, N., & Petitgirard, S. (2020). Experimental evidence for silica–enriched Earth's lower mantle with ferrous iron dominant bridgmanite. *Proceedings of the National Academy of Sciences of the United States of America*, *117*, 27899–27905. https://doi.org/10.1073/pnas.1917096117

Mori, Y., Ozawa, H., Hirose, K., Sinmyo, R., Tateno, S., Morard, G., & Ohishi, Y. (2017). Melting experiments on Fe–Fe_3S system to 254 GPa. *Earth and Planetary Science Letters*, *464*, 135–141. https://doi.org/10.1016/j.epsl.2017.02.021

Murakami, M., Hirose, K., Kawamura, K., Sata, N., & Ohishi, Y. (2004). Post-perovskite phase transition in $MgSiO_3$. *Science*, *304*, 855–858. DOI:10.1126/science.1095932

Murakami, M., Hirose, K., Sata, N., & Ohishi, Y. (2005). Post-perovskite phase transition and crystal chemistry in the pyrolitic lowermost mantle. *Geophysical Research Letters*, *32*, L03304. http://dx.doi.org/10.1029/2004GL021956

Murakami, M., Ohishi, Y., Hirao, N., & Hirose, K. (2012). A perovskitic lower mantle inferred from high-pressure, high-temperature sound velocity data. *Nature*, *485*, 90–94. https://doi.org/10.1038/nature11004

Nakagawa, T. & Tackley, P. J. (2004). Effects of a perovskite–post perovskite phase change mantle boundary in compressible mantle. *Geophysical Research Letters*, *31*, L16611. http://dx.doi.org/10.1029/2004GL020648

Nakagawa, T. & Tackley, P. J. (2011). Effects of low-viscosity post-perovskite on thermo- chemical mantle convection in a 3-D spherical shell. *Geophysical Research Letters*, *38*, L04309. http://dx.doi.org/10.1029/2010GL046494

Nomura, R., Hirose, K. Uesugi, K. Ohishi, Y., Tsuchiyama, A., Miyake, A., & Ueno, Y. (2014). Low core-mantle boundary temperature inferred from the solidus of pyrolite. *Science*, *343*, 522–525. DOI: 10.1126/science.1248186

Oganov, A. R. & Ono, S. (2004). Theoretical and experimental evidence for a post-perovskite phase of $MgSiO_3$ in Earth's D" layer. *Nature*, *430*, 445–448. DOI: 10.1038/nature02701

Ohta, K., Hirose, K., Lay, T., Sata, N., & Ohishi, Y. (2008). Phase transitions in pyrolite and MORB at lowermost mantle conditions: Implications for a MORB-rich pile above the core-mantle boundary. *Earth and Planetary Science Letters*, *267*, 107–117. https://doi.org/10.1016/j.epsl.2007.11.037

Ono, S. & Oganov, A. R. (2005). In situ observations of phase transition between perovskite and $CaIrO_3$-type phase in $MgSiO_3$ and pyrolitic mantle composition. *Earth and Planetary Science Letters*, *236*, 914–932. DOI:10.1016/j.epsl.2005.06.001

Pisconti, A., Thomas, C., & Wookey, J. (2019). Discriminating between causes of D" anisotropy using reflections and splitting measurements for a single path. *Journal of Geophysical Research: Solid Earth, 124*, 4811-4830. https://doi.org/10.1029/2018JB016993

Seto, Y., Nishio-Hamane, D., Nagai, T., & Sata, N. (2010). Development of a software suite on X-ray diffraction experiments. *Review of High Pressure Science and Technology*, *20*, 269–276. https://doi.org/10.4131/jshpreview.20.269

Shim, S., Duffy, T. S., & Takemura, K. (2002). Equation of state of gold and its application to the phase boundaries near 660 km depth in the Earth's mantle. *Earth and Planetary Science Letters, 203*, 729–739. https://doi.org/10.1016/S0012-821X(02)00917-2

Sinmyo, R., Hirose, K, Muto, S., Ohishi, Y., & Yasuhara, A. (2011). The valence state and partitioning of iron in the Earth's lowermost mantle. *Journal of Geophysical Research*, *116*, B07205. http://dx.doi.org/10.1029/2010JB008179

Speziale, S., Zha, C., Duffy, T.S., Hemley, R. J., & Mao, H. K. (2001). Quasi-hydrostatic compression of magnesium oxide to 52 GPa: implications for the pressure–volume–temperature equation of state. *Journal of Geophysical Research*, *106*, 515–528. https://doi.org/10.1029/2000JB900318

Tackley, P. J., Nakagawa, T., & Hernlund, J. W. (2007). Influence of the post-perovskite transition on thermal and thermo-chemical mantle convection. In K. Hirose, J. Brodholt, T. Lay, D. Yuen (Eds.), *Post-perovskite: the last mantle phase transition*, *Geophysical Monograph Series* (Vol. 174, pp. 229-247). Washington, DC: American Geophysical Union. http://dx.doi.org/10.1029/ 174GM11

Takahashi, E. (1986). Melting of a dry peridotite KLB-1 up to 14 GPa: implications on the origin of peridotite upper mantle. *Journal of Geophysical Research*, *91*, 9367–9382. https://doi.org/10.1029/JB091iB09p09367

Tateno, S., Hirose, K., Sata, N., & Ohishi, Y. (2005). Phase relations in $Mg_3Al_2Si_3O_{12}$ to 180 GPa: effect of Al on post-perovskite phase transition. *Geophysical Research Letters*, *32*, L15306. http://dx.doi.org/10.1029/2005GL023309

Tateno, S., Hirose, K., Sata, N., & Ohishi, Y. (2009). Determination of post-perovskite phase transition boundary up to 4,400 K and implications for thermal structure in D" layer. *Earth and Planetary Science Letters*, *277*, 130–136. https://doi.org/10.1016/J.EPSL.2008.10.004

Tateno, S., Hirose, K., & Ohishi, Y. (2014). Melting experiments on peridotite to lowermost mantle conditions. *Journal of Geophysical Research: Solid Earth, 119*, 4684–4694. https://doi.org/10.1002/2013JB010616

Tateno, S., Hirose, K., Sinmyo, R., Morard, G., Hirao, N., & Ohishi, Y. (2018a). Melting of Fe–Si–S alloys to core pressures: silicon in the core? *American Mineralogist*, *103*, 742–748. https://doi.org/10.2138/am-2018-6299

Tateno, S., Hirose, K., Sakata, S., Yonemitsu, K., Ozawa, H., Hirata, T., et al. (2018b). Melting phase relations and element partitioning in MORB to lowermost mantle conditions. *Journal of Geophysical Research: Solid Earth*, *123*, https://doi.org/10.1029/2018JB015790

Thomas, C., Kendall, J. M., & Lowman, J. (2004b). Lower-mantle seismic discontinuities and the thermal morphology of subducted slabs. *Earth and Planetary Science Letters, 225*, 105–113. doi:10.1016/j.epsl.2004.05.038

Townsend, J. P., Tsuchiya, J., Bina, C. R., & Jacobsen, S. D. (2016). Water partitioning between bridgmanite and postperovskite in the lowermost mantle. *Earth and Planetary Science Letters*, *454*, 20–27. http://dx.doi.org/10.1016/j.epsl.2016.08.009

Tsuchiya, T., (2003). First-principles prediction of the *P–V–T* equation of state of gold and the 660-km discontinuity in Earth's mantle. *Journal of Geophysical Research*, *108*, https://doi.org/10.1029/2003JB002446

Tsuchiya, T., Tsuchiya, J., Umemoto, K., & Wentzcovitch, R. M. (2004). Phase transition in $MgSiO_3$ perovskite in the Earth's lower mantle. *Earth and Planetary Science Letters*, *224*, 241–248. https://doi.org/10.1016/j.epsl.2004.05.017

Weber, M., Davis, J. P., Thomas, C., Krüger, F., Scherbaum, F., Schlittenhardt, J., & Körnig, M. (1996). The structure of the lowermost mantle as determined from using seismic arrays. In E. Boschi, G. Ekström, A. Morelli (Eds.), *Seismic modelling of the Earth's structure* (pp. 399–442). Rome: Instituto Nazionale di Geophysica.

Wysession, M. E., Lay, T., Revenaugh, J., Williams, Q., Garnero, E. J., Jeanloz, R., Kellogg, L. H. (1998). The D" discontinuity and its implications. In M. Gurnis, M.E. Wysession, E. Knittle, B.A. Buffett (Eds.), *The core-mantle boundary region*, *Geodynamical Series* (Vol. 28, pp. 273–297). Washington, DC: American Geophysical Union.

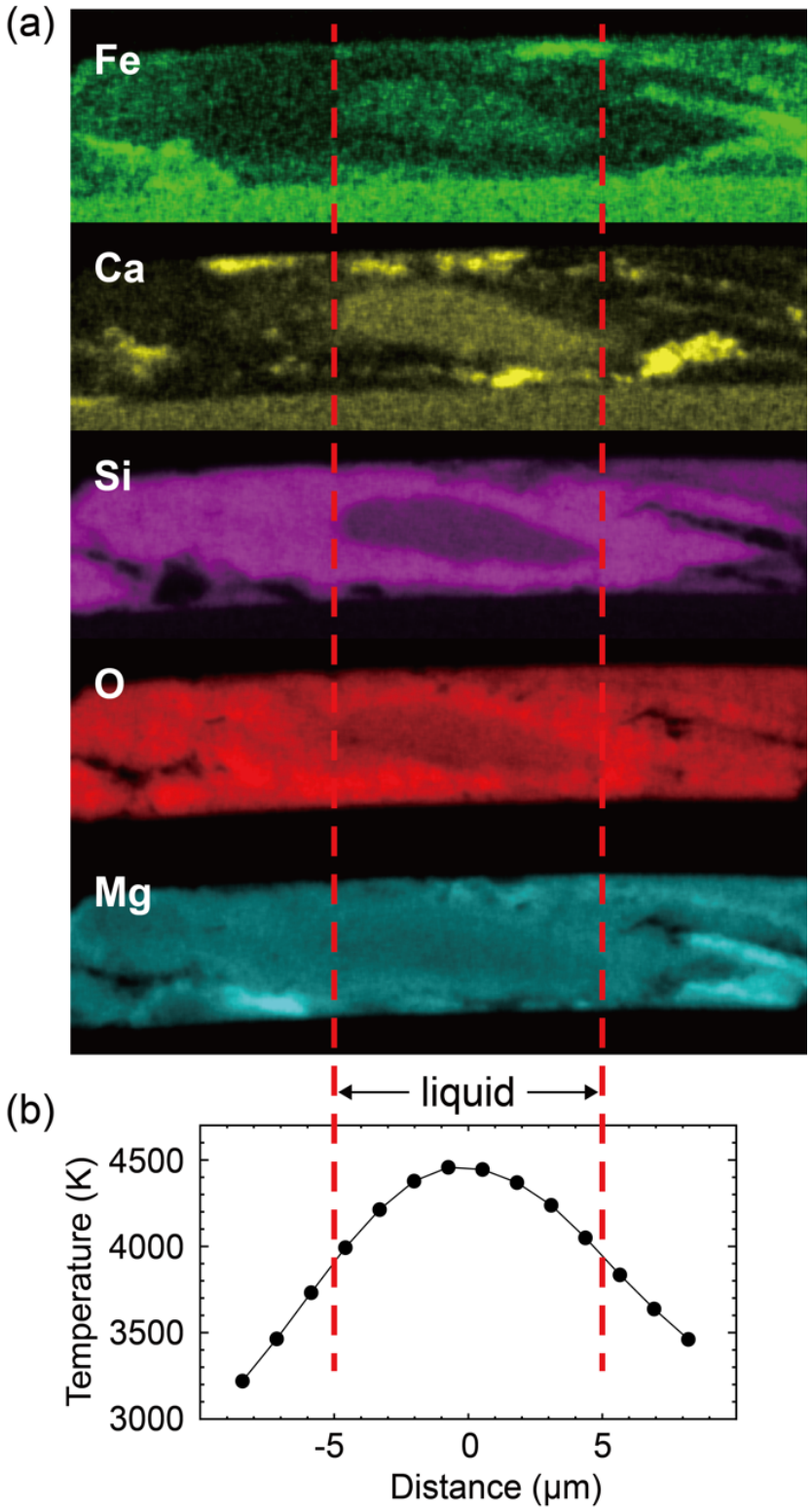

538

539 **Figure 1.** (a) X-ray elemental maps of the sample cross section recovered from run #1 at
540 122 GPa and 3910 K. (b) A corresponding temperature profile across the hot spot.

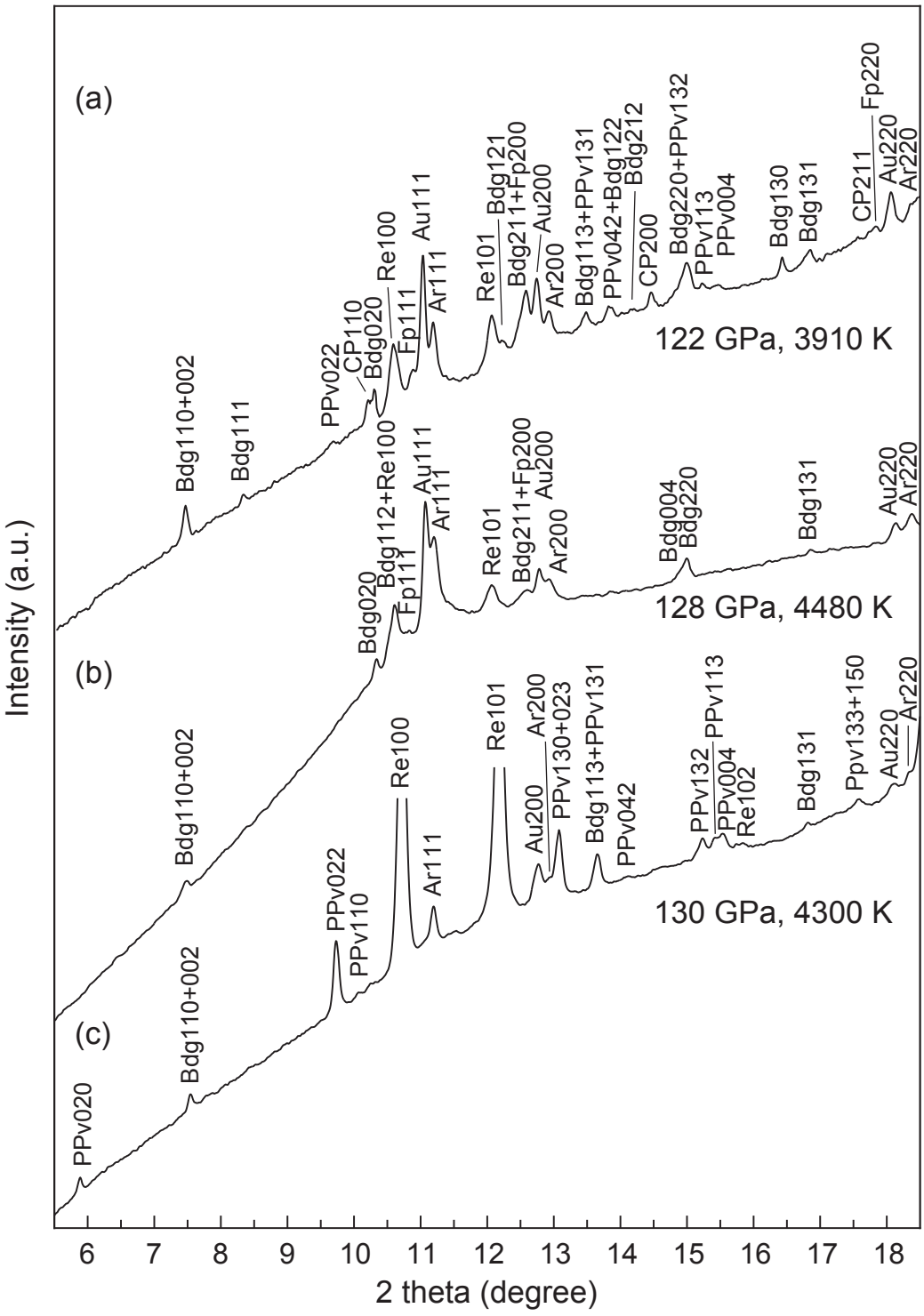

Figure 2. X-ray diffraction patterns at (a) 122 GPa and 3910 K, (b) 128 GPa and 4480 K, and (c) 130 GPa and 4300 K. Bdg, $MgSiO_3$-rich perovskite; PPv, post-perovskite; Fp, ferropericlase; CP, $CaSiO_3$ perovskite; Au, gold; Ar, argon pressure medium; Re, rhenium gasket.

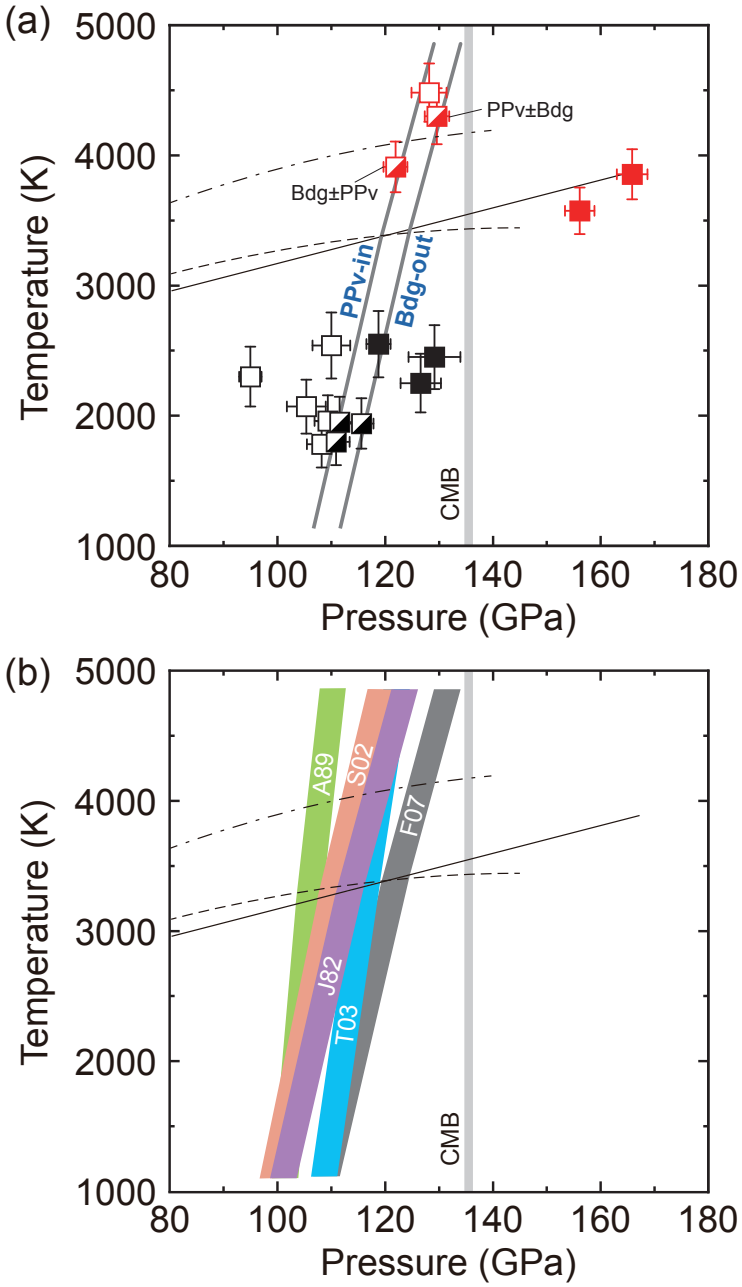

Figure 3. (a) Phase boundary between bridgmanite (Bdg) and post-perovskite (PPv). Open and solid symbols represent the stabilities of bridgmanite and post-perovskite, respectively. Half-filled symbols show the coexistence of both phases. Red symbols, this study; black symbols, from Ohta et al. (2008). Solid, broken, and dashed-dotted curves indicate solidus temperatures of pyrolite reported by Nomura et al. (2014), Kim et al. (2020), and Fiquet et al. (2010), respectively. (b) Changes in the phase boundary by using different EoSs of gold to calculate experimental pressures (Jamieson et al., 1982; Anderson et al., 1989; Shim et al., 2002; Tsuchiya, 2003; Fei et al., 2007).

555

556 **Table 1**

557 *Experimental Results*

Run#	Volume of Au ($Å^3$)	Pressure (GPa)	Temperature (K)	Phase assemblage
This study				
#1	52.19(5)	121.9(2)	3910	Bdg + PPv (trace) + Fp + CaPv + melt
#2	52.06(12)	128.1(3)	4480	Bdg + Fp + melt
#3	51.82(4)	129.6(2)	4300	PPv + Bdg (trace) + melt
#4	49.08(8)	165.9(3)	3860	PPv + Fp + CaPv
#5	49.53(8)	156.1(3)	3570	PPv + Fp + CaPv
Ohta et al. (2008)				
#1-1	51.91(11)	108.2(3)	1780	Bdg + Fp + CaPv
#1-2	51.93(7)	109.4(2)	1960	Bdg + Fp + CaPv
#1-3	52.26(12)	110.0(3)	2540	Bdg + Fp + CaPv
#2-1	51.70(8)	110.9(2)	1800	Bdg + PPv (trace) + Fp + CaPv
#2-2	51.75(9)	111.6(3)	1950	Bdg + PPv (trace) + Fp + CaPv
#3	51.43(6)	115.6(2)	1940	PPv + Bdg + Fp + CaPv
#4	53.43(3)	95.0(2)	2300	Bdg + Fp + CaPv
#5	52.33(17)	105.4(3)	2070	Bdg + Fp + CaPv
#6	51.56(1)	118.8(2)	2550	PPv + Fp + CaPv
#7	50.79(14)	126.6(4)	2250	PPv + Fp + CaPv
#8	50.72(20)	129.1(4)	2450	PPv + Fp + CaPv

The numbers in parentheses represent one standard deviation in the last digits.

Bdg, bridgmanite; PPv, post-perovskite; Fp, ferropericlase; CaPv, $CaSiO_3$ perovskite

558